Materials & Design 234 (2023) 112341

Contents lists available at ScienceDirect

Materials & Design

journal homepage: www.elsevier.com/locate/matdes

Nanoscale precipitation, mechanical properties, and deformation behavior of NiAl-strengthened high-strength steels: Effects of Ni and Al contents and ratios

B.C. Zhou [a,b], S.F. Liu [c], H.H. Wu [d], J.H. Luan [e], J.M. Guo [a,b], T. Yang [e], Z.B. Jiao [a,b,*]

[a] Department of Mechanical Engineering, Research Institute for Advanced Manufacturing, The Hong Kong Polytechnic University, Hong Kong, China
[b] The Hong Kong Polytechnic University Shenzhen Research Institute, Shenzhen 518057, China
[c] Department of Mechanical Engineering, City University of Hong Kong, Hong Kong, China
[d] School of Materials Science and Engineering, University of Science and Technology Beijing, Beijing 100083, China
[e] Inter-University 3D Atom Probe Tomography Unit, Department of Materials Science and Engineering, City University of Hong Kong, Hong Kong, China

ARTICLE INFO

Keywords:
High-strength steel
NiAl precipitate
Precipitation strengthening
Deformation
Ductility

ABSTRACT

Effects of Ni and Al contents and ratios on the continuous and discontinuous precipitation, mechanical properties, and deformation behavior of NiAl-strengthened steels were systematically studied through a combination of 3D atom probe tomography (APT), transmission electron microscopy (TEM), mechanical tests, and first-principles calculations. Microstructural analyses reveal that increasing the Ni and Al contents results in grain refinement and an increase in chemical potential gradient, both of which promote the discontinuous precipitation. The NiAl-strengthened steels with different Ni and Al contents and ratios exhibit high tensile strengths of 1000–1500 MPa but significantly different ductilities and fracture behaviors. TEM analyses indicate that fine-sized precipitates are sheared by moving dislocations, which leads to the formation of intersecting slip bands, thereby enhancing the work hardening capability. In contrast, coarse-sized discontinuous precipitates are bypassed by dislocations, resulting in a low rate of dislocation storage and hence low work hardening rate. In addition, increasing the Ni/Al ratio changes the fracture mode from brittle cleavage to ductile failure and improves the ductility of the Fe–Ni–Al steels. Microstructural analyses indicate that the ductilizing mechanisms are related to the increased bulk to shear modulus ratio (B/G) and the refined grain structure.

1. Introduction

High-strength low-carbon steels are of technological importance for many applications, including automotive, aerospace, shipbuilding, and construction industries [1–5]. NiAl precipitation strengthening has been proven to be one of the most effective approaches to strengthen low-carbon steels [6–10]. NiAl has a B2-ordered structure with a lattice parameter close to that of body-centered cubic (BCC) Fe [11], thus that NiAl precipitates are capable of high coherency with the BCC matrix and can precipitate on a sufficiently fine scale (less than 5 nm in diameter) to provide superior strengthening effects. Through appropriate composition design and heat treatments, high densities ($>10^{24}$ m^{-3}) of NiAl nanoparticles can uniformly precipitate in the matrix, which allows for the development of advanced steels with an ultrahigh strength of up to 2 GPa [11,12].

The precipitation strengthening response is highly dependent on the precipitate microstructures, including the precipitate morphology, size, number density, spatial distribution, and volume fraction [13–17]. The microstructures are in turn determined by the alloy composition, especially the concentration of precipitate-forming elements. Unlike conventional precipitation-strengthened steels that usually contain a small amount of precipitate-forming elements, NiAl precipitation-strengthened steels comprise a considerable amount of Ni and Al for achieving a sufficient amount of precipitates, because both Ni and Al have a substantial solubility in BCC Fe at intermediate temperatures [18]. From literature, it is noticed that the Ni and Al contents vary significantly in NiAl-strengthened steels, occupying a wide composition domain (3–18 wt% Ni and 1–10 wt% Al) [19–23]. The broad range of compositions results in a significant variation in the precipitate composition, microstructure, and mechanical properties of NiAl-

* Corresponding author at: Department of Mechanical Engineering, Research Institute for Advanced Manufacturing, The Hong Kong Polytechnic University, Hong Kong, China.
E-mail address: zb.jiao@polyu.edu.hk (Z.B. Jiao).

https://doi.org/10.1016/j.matdes.2023.112341
Received 18 April 2023; Received in revised form 3 September 2023; Accepted 19 September 2023
Available online 20 September 2023

strengthened steels. Previous studies indicate that the precipitate morphology of NiAl-strengthened steels is very sensitive to the Ni and Al contents. One reason that leads to the complexity of the precipitate morphology is that there are two modes of NiAl precipitation, namely continuous precipitation (CP) and discontinuous precipitation (DP) [24]. CP refers to the uniform precipitation of spherical NiAl nanoparticles in the matrix, whereas DP leads to the formation of coarse-sized NiAl rods near grain boundaries. Generally, a complete CP microstructure containing a high number density of spherical nanoparticles can be observed in steels with low Ni and Al contents, such as Fe–2.5Ni–1.5Al and Fe–5Ni–1Al (wt.%) steels [25,26], whereas a DP-dominant microstructure containing rod-like NiAl precipitates was reported in a Fe–8Ni–2Al (wt.%) steel [24]. The variations in the precipitate microstructure have a significant impact on the mechanical properties of NiAl-strengthened steels, especially the ductility. For example, Cho *et al.* [19] reported that a Fe–6.7Ni–5.8Al-based (wt.%) steel suffers from poor ductility and fractures in the elastic region. Teng *et al.* [21,22] also observed serious embrittlement in the NiAl-strengthened ferritic superalloys containing 3–10 wt% Al, and they also found that increasing the Al content results in a decrease in the ductility. In contrast, a good combination of high strength and ductility was often obtained in NiAl-strengthened steels with low Al contents, such as the Fe–18Ni–3Al- and Fe–8Ni–2Al-based (wt.%) steels [11,12,24]. Notably, Jiang *et al.* [12] reported that increasing the Al content of the Fe–18Ni–*x*Al-based (wt.%) steels enhances the strain hardening and improves the uniform ductility of the steels. Consequently, it appears that the precipitate microstructure, and mechanical properties of NiAl-strengthened steels are very sensitive to the Ni and Al contents, and some studies on the ductility of NiAl-strengthened steels are even inconsistent with each other [11,12,19,21,22,24], implying that it is not one single factor, but rather the combination of several factors that control the ductility. Although the effect of alloying elements on the microstructure and mechanical properties of low-carbon steels have been studied extensively, most studies focused on continuous precipitates (spherical particles) [12,19–23], and very little is known about discontinuous precipitates (rod-like precipitates) in NiAl-strengthened steels. Our previous study suggested that DP can be the dominant precipitation mode and occur concurrently with recrystallization, which results in the formation of high-density nanoprecipitation and ultrafine grains [14]. Moreover, DP is closer to the equilibrium state as compared with CP, which may lead to higher volume fraction of precipitates. Therefore, understanding the precipitation mechanism, mechanical properties, and plastic deformation behavior of NiAl-strengthened steels is essential. Several open questions remain, including: 1) What are the key metallurgical factors governing the continuous and discontinuous precipitation modes in NiAl-strengthened steels? 2) What are the mechanisms of dislocation interactions with continuous and discontinuous precipitates in NiAl-strengthened steels? 3) What mechanisms control the ductility and ductile-to-brittle transition of NiAl-strengthened steels? Addressing these questions is of paramount importance for understanding the composition-microstructure-property relationship and designing advanced NiAl-strengthened steels with superior mechanical properties.

In this study, we aim to fundamentally understand the effects of Ni and Al contents and ratios on the precipitate microstructure, mechanical properties, deformation mechanisms, and fracture behavior of NiAl-strengthened steels with a wide range of compositions. Specifically, we chose Fe–*x*Ni–3Al and Fe–8Ni–*y*Al ($x = 3 - 15$ and $y = 1 - 3$, wt.%) as the model alloys, and their multiscale microstructure from atomic to microscopic scales and mechanical properties were systematically studied through a combination of TEM, scanning electron microscopy (SEM), APT, EBSD, first-principles calculations, and mechanical tests. Particular effort was made to mechanistically understand the precipitation and deformation mechanisms of NiAl precipitates as well as the key factors controlling the ductility of NiAl-precipitation-strengthened steels.

2. Experimental and computational methods

Eight model alloys with nominal compositions of Fe–*x*Ni–3Al and Fe–8Ni–*y*Al ($x = 3 - 15$ and $y = 1 - 3$, wt.%) were studied. Chemical compositions of these steels measured by chemical analysis are given in Table 1. For simplicity, these alloys are designated according to their nominal Ni and Al concentrations in wt.%, i.e., 3Ni3Al, 5Ni3Al, 8Ni1Al, 8Ni2Al, 8Ni3Al, 10Ni3Al, 12Ni3Al, and 15Ni3Al. These alloys were fabricated by arc-melting a mixture of commercially pure metals (purity $\geq$ 99.9%) in an arc-melting furnace under a high-purity argon atmosphere. The ingots were re-melted four times to ensure chemical homogeneity and drop-cast into a copper mold with a cavity of $50 \times 15 \times 3$ mm^3. The as-cast ingots were cold-rolled with a total reduction of 67% to a final thickness of 1 mm. The rolled samples were solutionized for 30 min at 900 °C, followed by water quenching and then isothermal aging for 2 h at 550 °C.

Microstructures of the heat-treated samples were characterized by SEM (FEI Scios), TEM (JEM 2100F), EBSD (PHI 710), and X-ray diffraction (XRD). SEM samples were mechanically polished to a final surface using 0.05 μm alumina particles and etched using a 4 vol% Nital solution. TEM samples were first mechanically ground to a thickness of 45 μm and then twin-jet electro-polished (Struers Tenupol-5) in a solution comprised of 10 vol% $HClO_4$ and 90 vol% C_2H_5OH at −20 °C. EBSD samples were mechanically polished to a final surface using 0.3 μm alumina particles and then electro-polished in a solution of HNO_3 (25%) and C_2H_5OH (75%) at a voltage of 20 V and −40 °C. EBSD examinations were performed in a scanning Auger nanoprobe with an EDAX OIM 6.0 detector, and the electron beam was operated at 15 kV and 10nA. EBSD data were processed using the EDAX OIM software. XRD samples were scanned from 30° to 90° with a scanning rate of 3°/min by using Cu Kα radiation. Needle-shaped samples required for APT were prepared by lift-outs and annular milled in an FEI Scios focused ion beam/scanning electron microscope (FIB/SEM). The APT measurements were performed in a LEAP^{TM} 5000XR instrument in voltage mode. The specimens were tested at a temperature of 50 K, a pulse repetition rate of 200 kHz, a pulse fraction of 0.2, and an ion collection rate of 0.5% ions per field evaporation pulse. The Image Visualization and Analysis Software version 3.8.2 was used for three-dimensional reconstructions, compositional analyses, and the creation of *iso*-concentration surfaces.

Room-temperature tensile tests were carried out on an MTS tensile machine at a strain rate of 10^{-3} s^{-1}. Dog-bone-shaped specimens with a cross-section of 3.2×1 mm^2 and a gauge length of 12.5 mm were prepared by electro-discharge machining and then grounded on each side with 2000-grit SiC papers. The yield strength was determined via the 0.2% offset plastic strain method. Fracture surfaces were examined by SEM.

Table 1
Chemical compositions of the studied steels measured by chemical analysis.

Steel	Ni (wt.%)	Al (wt.%)	Si (wt.%)	Mn (wt.%)	C (wt.%)	Fe (wt.%)
3Ni3Al	2.87 ± 0.06	2.91 ± 0.05	0.02 ± 0.01	0.01 ± 0.01	0.02 ± 0.01	balance
5Ni3Al	4.79 ± 0.08	3.00 ± 0.09	0.06 ± 0.02	0.01 ± 0.01	0.03 ± 0.01	balance
8Ni3Al	7.92 ± 0.12	2.83 ± 0.03	0.07 ± 0.03	0.02 ± 0.01	0.02 ± 0.01	balance
10Ni3Al	9.92 ± 0.22	3.03 ± 0.10	0.05 ± 0.02	0.04 ± 0.01	0.02 ± 0.01	balance
12Ni3Al	11.93 ± 0.02	3.02 ± 0.02	0.05 ± 0.03	0.01 ± 0.01	0.02 ± 0.01	balance
15Ni3Al	14.95 ± 0.32	2.95 ± 0.08	0.06 ± 0.01	0.01 ± 0.01	0.01 ± 0.01	balance
8Ni1Al	7.86 ± 0.05	0.95 ± 0.03	0.02 ± 0.01	0.01 ± 0.01	0.02 ± 0.01	balance
8Ni2Al	7.85 ± 0.07	1.94 ± 0.03	0.03 ± 0.01	0.01 ± 0.01	0.02 ± 0.01	balance

First-principles calculations were performed in the framework of density functional theory implemented in the Vienna *ab initio* Simulation Package (VASP) with project augmented wave (PAW) method and the Perdew-Becke-Erzenhof exchange–correlation functional [27–29]. Three-dimensional 128-atom periodic supercells with 4 × 4 × 4 unit cells and 32-atom periodic supercells with 2 × 2 × 4 unit cells were constructed to determine the formation energy and elastic constant, respectively. The plane-wave energy cutoff was set at 450 eV, and the k-point mesh of 4 × 4 × 4 was adopted.

3. Results

3.1. Grain structure

The SEM microstructures of the Fe-*x*Ni-3Al and Fe-8Ni-*y*Al steels after aging for 2 h at 550 °C are displayed in Fig. 1. The micrographs reveal regions with dark and bright contrast, representing the CP and DP regions, respectively. The DP region containing rod-like precipitates shows a brighter contrast relative to the CP region containing nano-sized spheroidal particles. The area fractions of DP regions in the Fe-*x*Ni-3Al and Fe-8Ni-*y*Al steels were evaluated from SEM micrographs and are summarized in Fig. 2a and b, respectively. The area fraction of DP regions was computed by dividing the sum of the DP region pixels to the total number of pixels in the image in the ImageJ software. For the Fe-*x*Ni-3Al steels, the area fraction of DP regions increases from 13% ± 7% in the 3Ni3Al steel, to 34% ± 8% in the 5Ni3Al steel, to 69% ± 5% in the 8Ni3Al steel, and to 90–95% in the 10Ni3Al and 12Ni3Al steels. In the 15Ni3Al steel, the DP develops throughout the whole sample, with no CP regions being observed. For the Fe-8Ni-*y*Al steels, the area fraction of DP regions increases from 15% ± 7% in the 8Ni1Al steel to 62% ± 8% in the 8Ni2Al steel and to 69% ± 5% in the 8Ni3Al steel. These observations indicate that increasing the Ni and/or Al contents promotes the DP

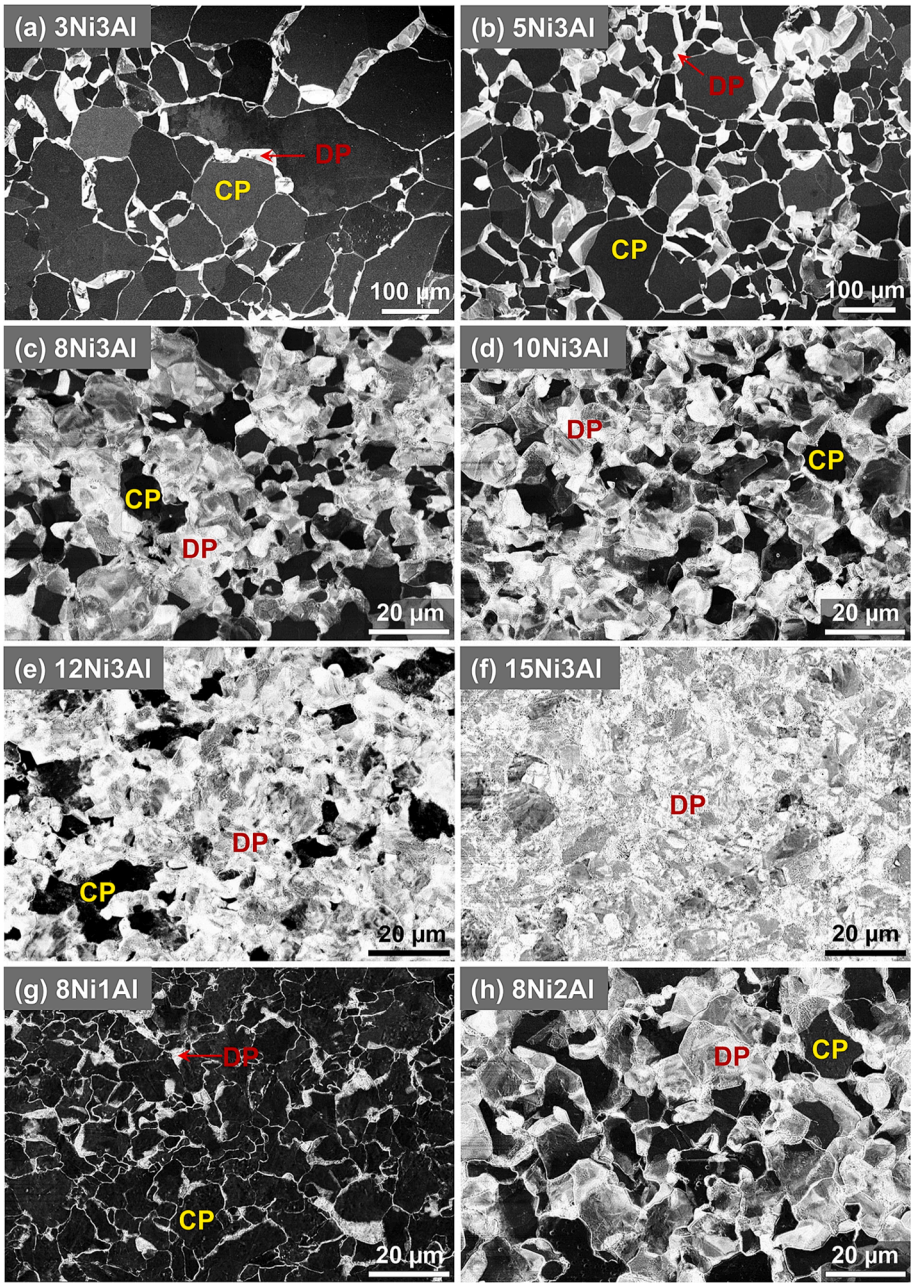

Fig. 1. Microstructures of the Fe-*x*Ni-3Al and Fe-8Ni-*y*Al steels after aging for 2 h at 550 °C: (a) 3Ni3Al, (b) 5Ni3Al, (c) 8Ni3Al, (d) 10Ni3Al, (e) 12Ni3Al, (f) 15Ni3Al, (g) 8Ni1Al, and (h) 8Ni2Al.

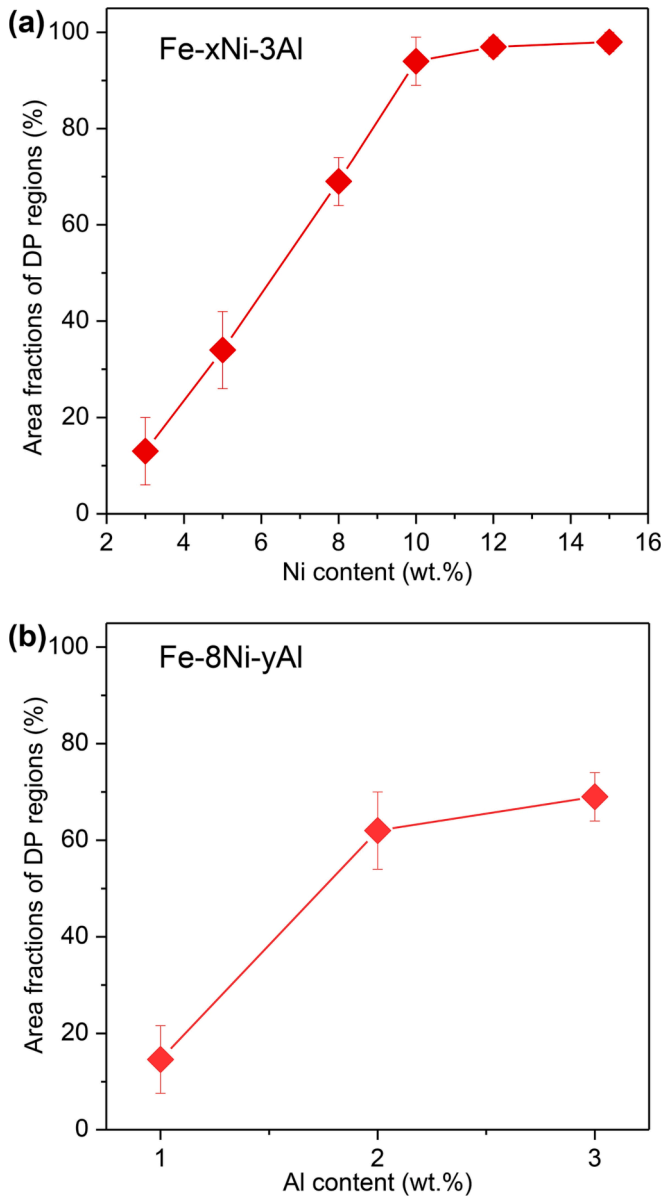

Fig. 2. The area fractions of DP regions in the (a) Fe–*x*Ni–3Al and (b) Fe–8Ni–*y*Al steels.

reaction of the Fe–Ni–Al steels.

The 3Ni3Al and 5Ni3Al steels exhibit coarse grains with average grain sizes of 84 ± 8 μm and 73 ± 10 μm, respectively. All other steels contain high fractions of DP regions, and their grain structures are not clearly resolved by SEM, which is related to the extensive migration of grain boundaries during the DP reaction [30,31]. To visually characterize the grain structures of these DP-dominant steels, EBSD measurements were performed. The inverse pole figure maps of the 3NiAl, 5Ni3Al, 8Ni3Al, 10Ni3Al, 12Ni3Al, 15Ni3Al, 8Ni1Al, and 8Ni2Al steels are displayed in Fig. 3a-j, respectively. It should be pointed out that all the steels exhibit a fully equiaxed ferritic structure with no detectable austenite phases. For comparison, the evolution of average grain sizes of the Fe-*x*Ni-3Al and Fe-8Ni-*y*Al steels are plotted in Fig. 3k and l, respectively. The grain size distribution histograms of the steels are displayed in Supplementary Fig. S1. It is evident that the average grain sizes of the 3Ni3Al and 5Ni3Al steels are more than 6 times over those of all other steels studied, suggesting that the Ni and Al contents in a certain range have a drastic effect on the grain size of the Fe–Ni–Al steels.

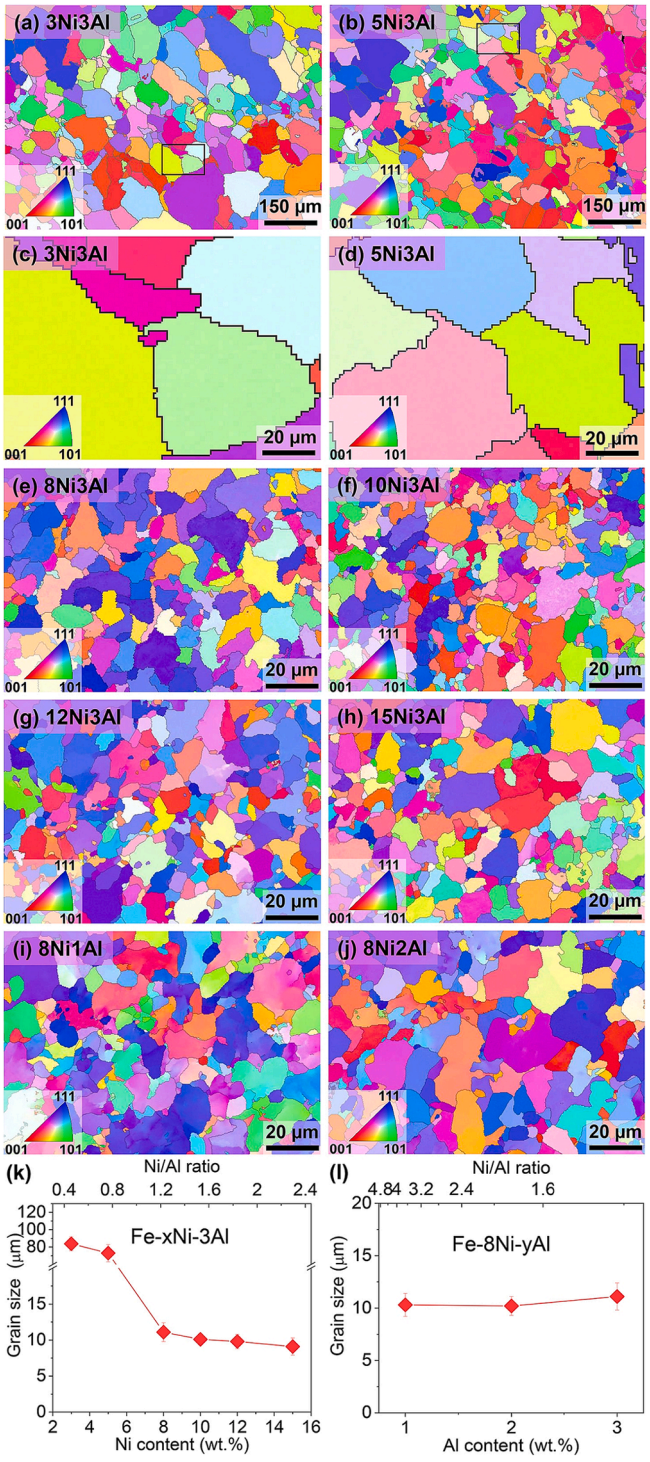

Fig. 3. EBSD inverse pole figure maps of the Fe–*x*Ni–3Al and Fe–8Ni–*y*Al steels in the 2-h aged condition: (a,c) 3Ni3Al, (b,d) 5Ni3Al, (e) 8Ni3Al, (f) 10Ni3Al, (g) 12Ni3Al, (h) 15Ni3Al, (i) 8Ni1Al, and (j) 8Ni2Al. (c) and (d) are enlarged view of the regions boxed in (a) and (b), respectively. (k) and (l) summarize the average grain sizes of the Fe-*x*Ni-3Al and Fe-8Ni-*y*Al steels, respectively.

3.2. Nanoscale precipitation

3.2.1. DP microstructure

TEM and APT were used to characterize the crystal structure, morphology, and composition of DP structures at the nanoscale. The dark-field TEM image and corresponding selected area electron diffraction (SAED) pattern of the DP region of the 8Ni3Al steel are

displayed in Fig. 4a and b, respectively. Highly aligned and parallel rod-like precipitates were clearly observed. The SAED pattern reveals the presence of superlattice reflection corresponding to a B2-ordered structure. The APT atom maps of the DP region of the 8Ni3Al steel are shown in Fig. 4c, which reveal the co-partitioning of Ni and Al to rod-like precipitates. The 12 at.% Al concentration isosurfaces were used to visualize the NiAl precipitates in the DP region, and the proximity histogram concentration profiles of Fe, Ni, and Al based on the iso-surfaces are illustrated in Fig. 4d. The NiAl rods are enriched in Ni (48.6 ± 0.9 at.%) and Al (44.6 ± 0.8 at.%) together with a small amount of Fe (6.7 ± 0.4 at.%), whereas the matrix of the DP region is depleted in Ni (2.0 ± 0.1 at.%) and Al (3.6 ± 0.1at.%). In addition, the DP microstructures of all other steels were also examined by APT, as displayed in Supplementary Fig. S2. The DP precipitate compositions of the Fe-*x*Ni-3Al and Fe-8Ni-*y*Al steels are summarized in Fig. 4e and f, respectively. For the DP precipitates in the Fe-*x*Ni-3Al steels, the Ni concentration increases from 48.4 ± 1.4 at.% in the 3Ni3Al steel to 52.4 ± 1.2 at.% in the 15Ni3Al steel, whereas the Al concentration decreases from 46.3 ± 1.5 at.% in the 3Ni3Al steel to 33.3 ± 0.8 at.% in the 15Ni3Al steel. For the DP precipitates in the Fe-8Ni-*y*Al steels, the Ni concentration decreases from 52.0 ± 1.8 at.% in the 8Ni1Al steel to 48.6 ± 0.9 at.% in the 8Ni3Al steel, whereas the Al concentration increases from 34.0 ± 1.5 at.% in the 8Ni1Al steel to 44.6 ± 0.8 at.% in the 8Ni3Al steel. The DP matrix composition of the Fe-*x*Ni-3Al and Fe-8Ni-*y*Al steels are displayed in Fig. 4g and h, respectively. For the matrix composition of the Fe-*x*Ni-3Al steel, the Ni concentration increases and the Al concentration decreases with an increasing Ni content. For the matrix composition of the Fe-8Ni-*y*Al steel, the Ni concentration decreases and the Al concentration increases with an increasing Al content. With the increase of the Ni/Al ratio, the Ni content in the matrix increases while the Al content decreases.

3.2.2. CP microstructure

To quantitatively characterize the precipitate microstructure of ultrafine CP nanoparticles, APT was performed on the CP regions of the Fe–Ni–Al steels. The 12 at.% Al *iso*-concentration surfaces were used to visualize the NiAl precipitates. The CP microstructures of the Fe–*x*Ni–3Al and Fe–8Ni–*y*Al steels are displayed in Fig. 5. Spheroidal nanoparticles were readily detected in all the samples except the 15Ni3Al steel, in which only rod-like NiAl precipitates can be observed (cf. Fig. 1f). The average radius, number density, and volume fraction of NiAl precipitates are summarized in Table 2. The 3Ni3Al and 8Ni1Al steels show relatively low volume fractions being 2.7% ± 0.8% and 2.3% ± 0.7%, respectively, which is likely due to the low Ni and Al contents in the two steels. With the increase of the Ni and Al contents, the volume fraction of precipitates increases gradually, reaching 7.4 ± 1.7% in the 12Ni3Al steel.

The CP precipitate and matrix compositions of the Fe–*x*Ni–3Al and Fe–8Ni–*y*Al steels were estimated using proximity histogram analysis, and the results are summarized in Fig. 6. In the precipitates of the Fe–*x*Ni–3Al steels, the Ni content increases from 32.4 ± 2.4 at.% in the 3Ni3Al steel to 49.1 ± 1.1 at.% in the 12Ni3Al steel, whereas the Al content decreases from 41.8 ± 2.5 at.% in the 3Ni3Al steel to 35.9 ± 1.1 at.% in the 12Ni3Al steel. As the Ni content increases, the precipitates become more enriched in Ni than Al, and Fe tends to partition to the precipitates by occupying the Al sublattice, thereby forming Ni(Al,Fe) precipitates. As a result, we observed that the CP precipitates exhibit a decrease in Al content with increasing Ni content. For the precipitates of the Fe–8Ni–*y*Al steels, the Ni content slightly decreases from 51.4 ± 2.4 at.% in the 8Ni1Al steel to 43.4 ± 2.7 at.% in the 8Ni3Al steel, while the Al content increases from 33.7 ± 1.3 at.% in the 8Ni1Al steel to 38.3 ± 2.6 at.% in the 8Ni3Al steel. In the matrix of the Fe–*x*Ni–3Al steels, the Ni concentration increases monotonously from 2.1 ± 0.1 at.% in the 3Ni3Al steel to 5.5 ± 0.2 at.% in the 12Ni3Al steel, whereas the Al concentration shows an opposite trend, decreasing gradually from 5.2 ± 0.1 at.% in the 3Ni3Al steel to 1.5 ± 0.1 at.% in the 12Ni3Al steel. It is worth noting that the volume fraction of NiAl precipitates in the Fe–*x*Ni–3Al steels increases with increasing Ni content, as summarized in Table 2. As such, more Al is consumed by the precipitates, leaving less Al in the matrix. As a result, the CP matrix exhibits a decrease in Al content with increasing Ni content. For the matrix of the Fe–8Ni–*y*Al steels, the Ni concentration decreases from 6.5 ± 0.1 at.% in the 8Ni1Al steel to 4.4 ± 0.3 at.% in the 8Ni2Al steel and to 3.9 ± 0.1 at.% in the 8Ni3Al steel, whereas the Al concentration increases from 1.2 ± 0.1 at.% in the 8Ni1Al steel to 1.7 ± 0.2 at.% in the 8Ni2Al steel and to 2.2 ± 0.1 at.% in the 8Ni3Al steel. The variation of the CP matrix composition with the Ni and Al contents has a similar trend as that of the DP matrix composition. From these data, it is evident that along with the precipitation of NiAl nanoparticles, the Ni and Al concentrations in the matrix vary significantly.

3.3. Mechanical properties

Room-temperature tensile tests were performed to investigate the effects of Ni and Al contents on the mechanical properties of the NiAl-strengthened steels. The representative engineering stress–strain curves of the Fe–*x*Ni–3Al and Fe–8Ni–*y*Al steels in the 2-h aged condition are displayed in Fig. 7a and b, respectively. The 3Ni3Al and 5Ni3Al steels are very brittle and fracture in the elastic region without measurable macro-plasticity. Except for these two steels, all others show both elastic and plastic deformations in the stress–strain curves. For the Fe–*x*Ni–3Al steels with × = 8–15 wt%, their yield strengths are quite similar, in the range of 1022–1165 MPa, whereas their ductilities vary significantly. The work hardening rate and true stress–strain curves of the Fe–*x*Ni–3Al and Fe–8Ni–*y*Al steels are displayed in Fig. 7c and d. It is evident that the 10Ni3Al steel achieves the highest work hardening rate in the early stage of plastic deformation, and the work hardening rate decreases with increasing the Ni content. With the increase of the Al content, the work hardening rate of the Fe–8Ni–*y*Al steels also increases. The elongation-to-failure of the Fe-*x*Ni-3Al steels are plotted in Fig. 7e as a function of Ni content. As the Ni content increases, the elongation-to-failure increases from 4% ± 2% for the 8Ni3Al steel, to 8% ± 1% for the 10Ni3Al steel, to 11% ± 1% for the 12Ni3Al steel, and to 15% ± 2% for the 15Ni3Al steel. By contrast, an opposite trend was observed with increasing Al content, as shown in Fig. 7f. With increasing Al content, the elongation-to-failure decreases from 14% ± 1% for the 8Ni1Al steel to 13% ± 1% for the 8Ni2Al steel and to 4% ± 1% in the 8Ni3Al steel. Increasing the Ni/Al ratio leads to the increase of the ductility of the Fe–Ni–Al steels. The results indicate that the Ni and Al contents and ratios in the bulk composition have a significant impact on the tensile ductility.

3.4. Fractography

Representative fracture surfaces of the Fe–*x*Ni–3Al and Fe–8Ni–*y*Al steels are displayed in Fig. 8. It is evident that the Ni content has a significant influence on the fracture mode of the Fe-*x*Ni-3Al steels. The 3Ni3Al and 5Ni3Al steels exhibit a mixture of transgranular cleavage and intergranular fracture, which is consistent with the brittle failure as observed in Fig. 7a. The 8Ni3Al steel exhibits primarily a transgranular cleavage-dominated fracture, but its cleavage facet sizes are much smaller than those of the 3Ni3Al and 5Ni3Al steels, which is likely related to the small grain size of the 8Ni3Al steel. In the 10Ni3Al steel, cleavage remains the main fracture mode, but a small fraction (2.4% ± 0.9%) of dimple marks appears, suggesting a transition from the brittle to ductile failure, in accordance with the improved elongation-to-failure as observed in Fig. 7a. As the Ni content increases to 12 wt%, the fraction of dimpled area increases to 5.5% ± 1.3%, showing enhanced ductile features. Further increasing the Ni addition to 15 wt% leads to a completely ductile fracture with fine-sized dimples, which is accompanied by an increase in the elongation-to-failure to 15% ± 2%. For the Fe-8Ni-*y*Al series, the fracture samples of the 8Ni1Al and 8Ni2Al steels

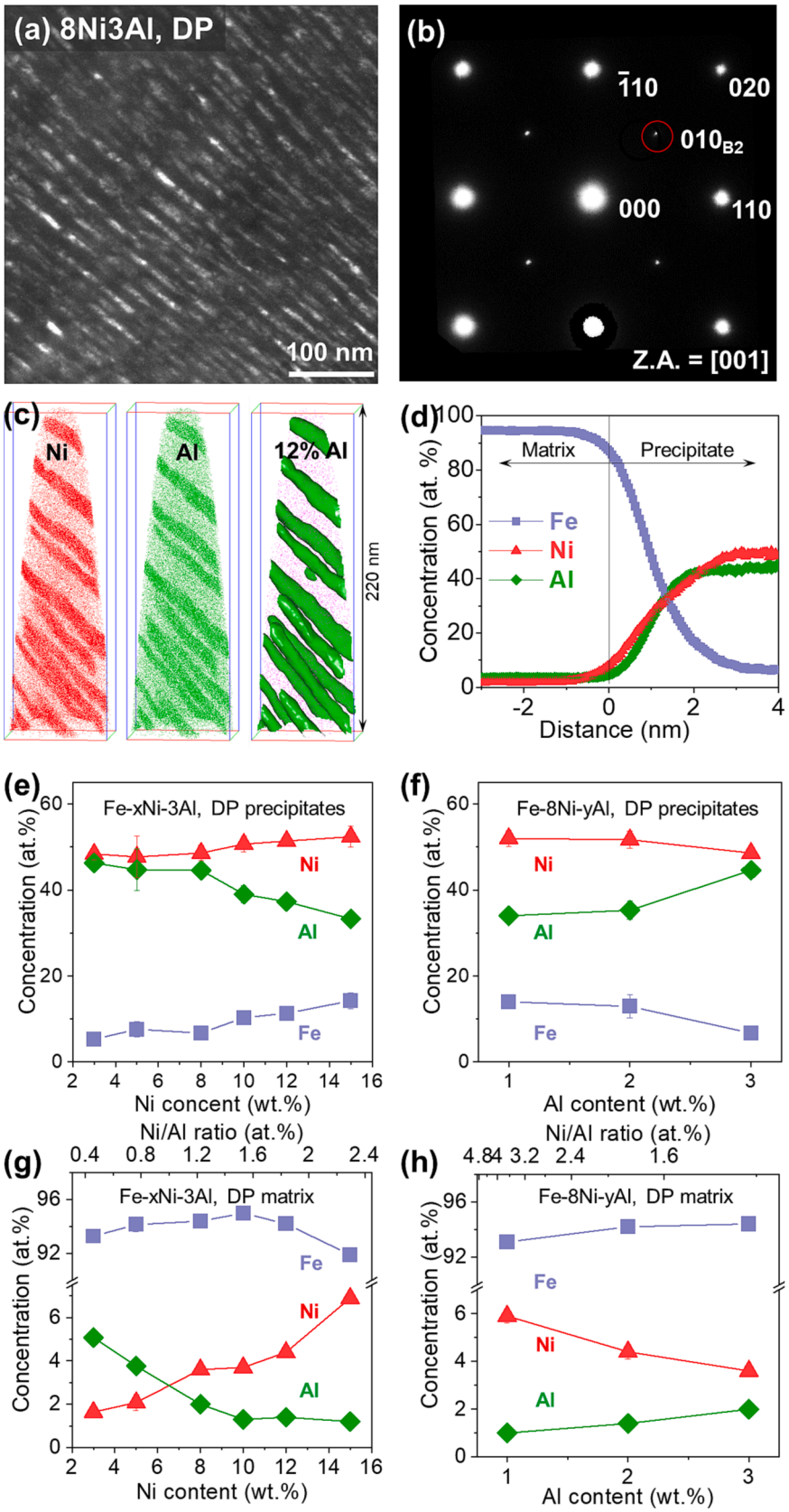

Fig. 4. DP microstructures of the 8Ni3Al steel: (a) representative dark-field TEM image, (b) SAED pattern, (c) APT atom maps and 12 at.% Al concentration iso-surfaces, and (d) proximity histogram concentration profiles of Fe, Ni, and Al. (e) and (f) are the DP precipitate compositions of the Fe–*x*Ni–3Al and Fe–8Ni–*y*Al steels, respectively, and (g) and (h) are the DP matrix compositions of the Fe-*x*Ni-3Al and Fe-8Ni-*y*Al steels, respectively.

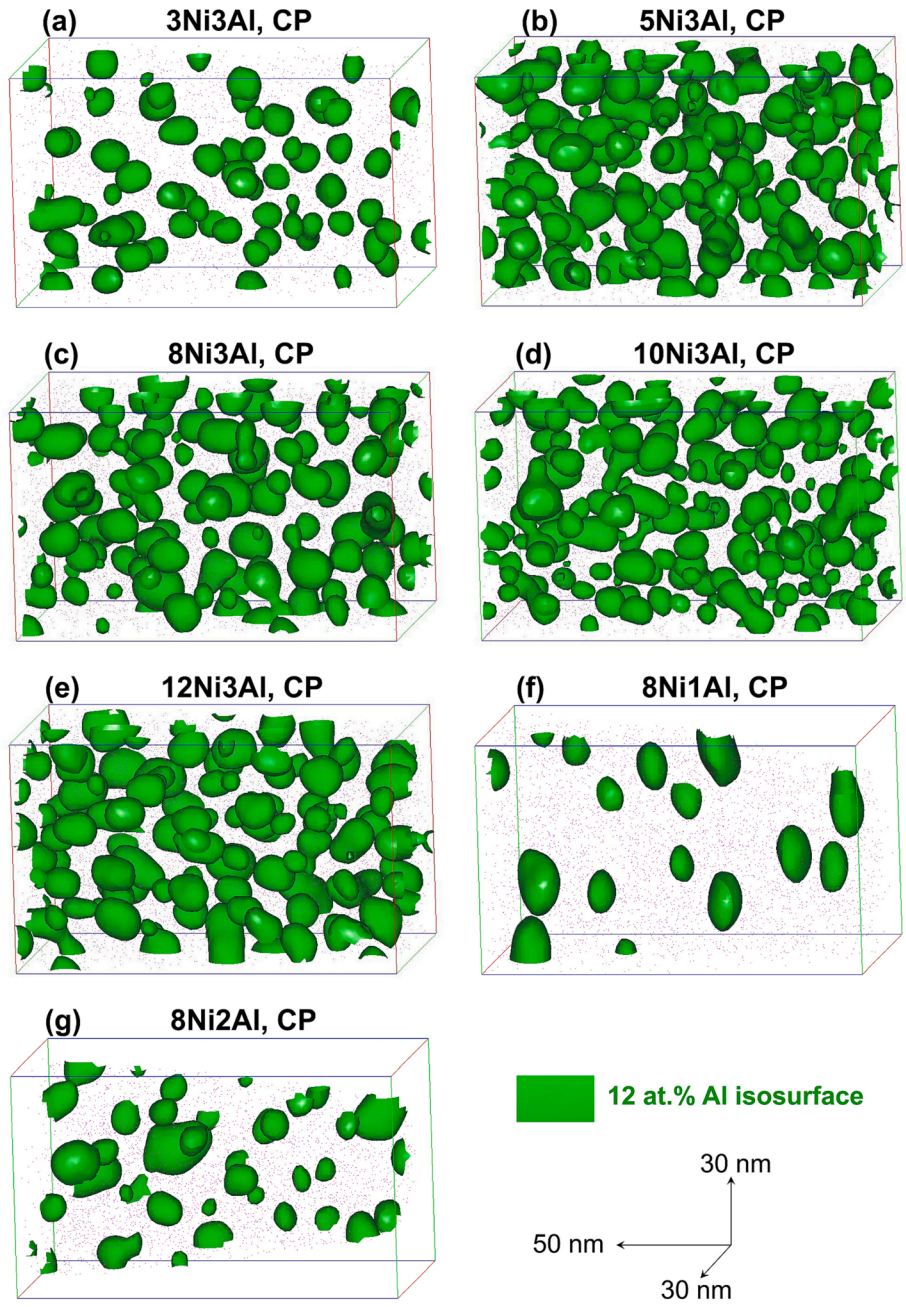

Fig. 5. CP microstructures of the Fe–Ni–Al steels: (a) 3Ni3Al, (b) 5Ni3Al, (c) 8Ni3Al, (d) 10Ni3Al, (e) 12Ni3Al, (f) 8Ni1Al, and (g) 8Ni2Al.

Table 2
Particle radii (R), number densities (N), and volume fractions (f) of nanoscale NiAl particles in the CP regions of the 3Ni3Al, 5Ni3Al, 8Ni3Al, 10Ni3Al, 12Ni3Al, 8Ni1Al, and 8Ni2Al steels in the 2-h aged condition.

Steel	R (nm)	N (m^{-3})	f (%)
3Ni3Al	1.7 ± 0.4	1.3×10^{24}	2.7 ± 0.8
5Ni3Al	1.9 ± 0.5	1.7×10^{24}	4.9 ± 2.0
8Ni3Al	1.9 ± 0.5	1.9×10^{24}	5.5 ± 1.7
10Ni3Al	1.7 ± 0.4	2.9×10^{24}	6.0 ± 2.0
12Ni3Al	2.1 ± 0.5	1.9×10^{24}	7.4 ± 1.7
8Ni1Al	2.7 ± 0.6	3.2×10^{23}	2.3 ± 0.7
8Ni2Al	1.6 ± 0.5	2.4×10^{24}	4.2 ± 1.9

exhibit fine dimples and obvious necking, indicating a typical ductile failure mode, which is significantly different from that of the 8Ni3Al steel (a transgranular cleavage-dominated fracture mode). These fracture characteristics are consistent with the aforementioned tensile results, further confirming that increasing the Ni content or Ni/Al ratio improves the alloy ductility, whereas increasing the Al content or decreasing the Ni/Al ratio deteriorates the alloy ductility.

4. Discussion

4.1. Effects of Ni and Al contents on the DP behavior

The microstructural results (Fig. 1) reveal that the volume fraction of DP regions increases with increasing Ni and/or Al contents. Fundamentally, DP cells initiate at grain boundaries and advance into grain interiors behind a moving grain boundary (known as the reaction front), ahead of which is the untransformed or continuously transformed matrix with a high supersaturation [30,32,33]. The driving force of the DP process is related to the grain boundary characteristic and chemical

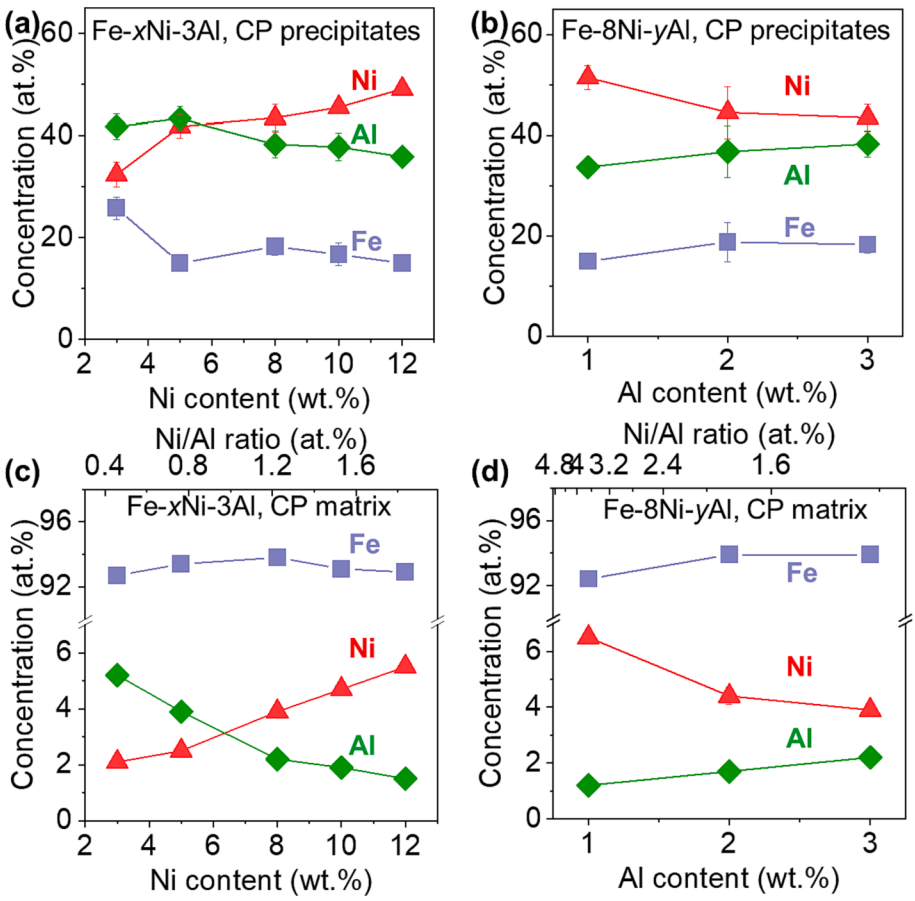

Fig. 6. CP precipitate compositions of the (a) Fe–*x*Ni–3Al and (b) Fe–8Ni–*y*Al steels, and CP matrix compositions of the (c) Fe–*x*Ni–3Al and (d) Fe–8Ni–*y*Al steels.

potential gradient across the reaction front. Therefore, the effects of Ni and Al contents on the DP reaction will be discussed in terms of the grain boundary characteristic and chemical potential gradient.

First, the Ni/Al ratio-dependent grain structure and its influence on the DP microstructure of the Fe–Ni–Al steels are discussed. In the Fe–Ni–Al system, Ni is an austenite stabilizer, which expands the austenite phase field, whereas Al is a ferrite stabilizer, which expands the ferrite phase zone [34]. Thus, the Ni and Al contents and ratios are expected to have a strong influence on the phase transformations of the Fe–Ni–Al steels. It is known that the grain size is closely related to the phase transformation temperatures; therefore, the Ni/Al ratio is likely to play an important role in determining the grain size of the steels. To quantitatively understand the influence of Ni/Al ratio on the phase transformations, thermodynamic calculations were performed. The phase diagrams of the Fe–*x*Ni–3Al and Fe–8Ni–*y*Al steels are displayed in Supplementary Fig. S3a and b, respectively. For the 3Ni3Al and 5Ni3Al steels, the ferrite phase zone is significantly expanded due to the low Ni/Al ratios. The recrystallization of the two alloys occurs in the ferrite phase region, with no ferrite/austenite transformations during the subsequent cooling. Thus, in these two steels the ferrite grains form at a high temperature of 900 °C during the recrystallization treatment, thereby resulting in the formation of coarse grain structures (average grain sizes of 80–90 μm). For the 8Ni3Al steel, although the recrystallization occurs in the dual-phase FCC + BCC region, the FCC phase is dominant (59% in volume fraction) at 900 °C. In contrast, for all other steels, the solution treatment occurs in the single-phase FCC region, and there are obvious transformations from austenite to α-ferrite at intermediate temperatures. In these cases, the solution treatment at 900 °C leads to the formation of austenite grains, which subsequently transform to fine-scale ferrite grains during the cooling process. As a result, fine grain structures (average grain sizes of 9–13 μm) were formed in the steels, which are significantly finer than those of the 3Ni3Al and 5Ni3Al steels. A decrease in the grain size leads to more grain boundaries that act as nucleation sites for DP, so the grain refinement contributes to an increase in the volume fraction of DP. To experimentally confirm the effect of grain size on the DP formation, we examined the DP microstructure of the 5Ni3Al steel with different initial grain sizes. From Supplementary Fig. S4, it is evident that as the grain size decreases from 73 ± 10 μm to 32 ± 8 μm and to 25 ± 7 μm, the area fraction of DP regions increases from 34% ± 8% to 47% ± 7% and 52% ± 5%, thereby experimentally confirming that a fine grain structure promotes the DP formation.

Second, the effects of Ni and Al contents on the chemical potential gradient are analyzed. CP and DP are two competitive modes to reduce the supersaturation of the matrix; the former continuously consumes the solute in the supersaturated matrix with time, whereas the latter induces an abrupt change in the solute concentration, resulting in a near-equilibrium composition of the matrix. The difference in the solute concentration between the CP and DP matrix provides the chemical driving force for the growth of DP cells. According to Petermann and Hornbogen [35], the chemical driving force for the DP reaction can be described by

$$\Delta G_{DP} = -RT\left(x_{CP}^{Fe}\ln\frac{x_{CP}^{Fe}}{x_{DP}^{Fe}} + x_{CP}^{Ni}\ln\frac{x_{CP}^{Ni}}{x_{DP}^{Ni}} + x_{CP}^{Al}\ln\frac{x_{CP}^{Al}}{x_{DP}^{Al}}\right) \quad (1)$$

where *xFe CP*, *xNi CP*, and *xAl CP* are respectively the Fe, Ni, and Al concentrations in the CP matrix, *xFe DP*, *xNi DP*, and *xAl DP* are respectively the Fe, Ni, and Al concentrations in the DP matrix, $R = 8.31$ J/K·mol is the gas constant, and $T = 823$ K is the temperature. Here we calculated the chemical driving force for the DP reaction in the very beginning of precipitation. It is known that the CP reaction continuously

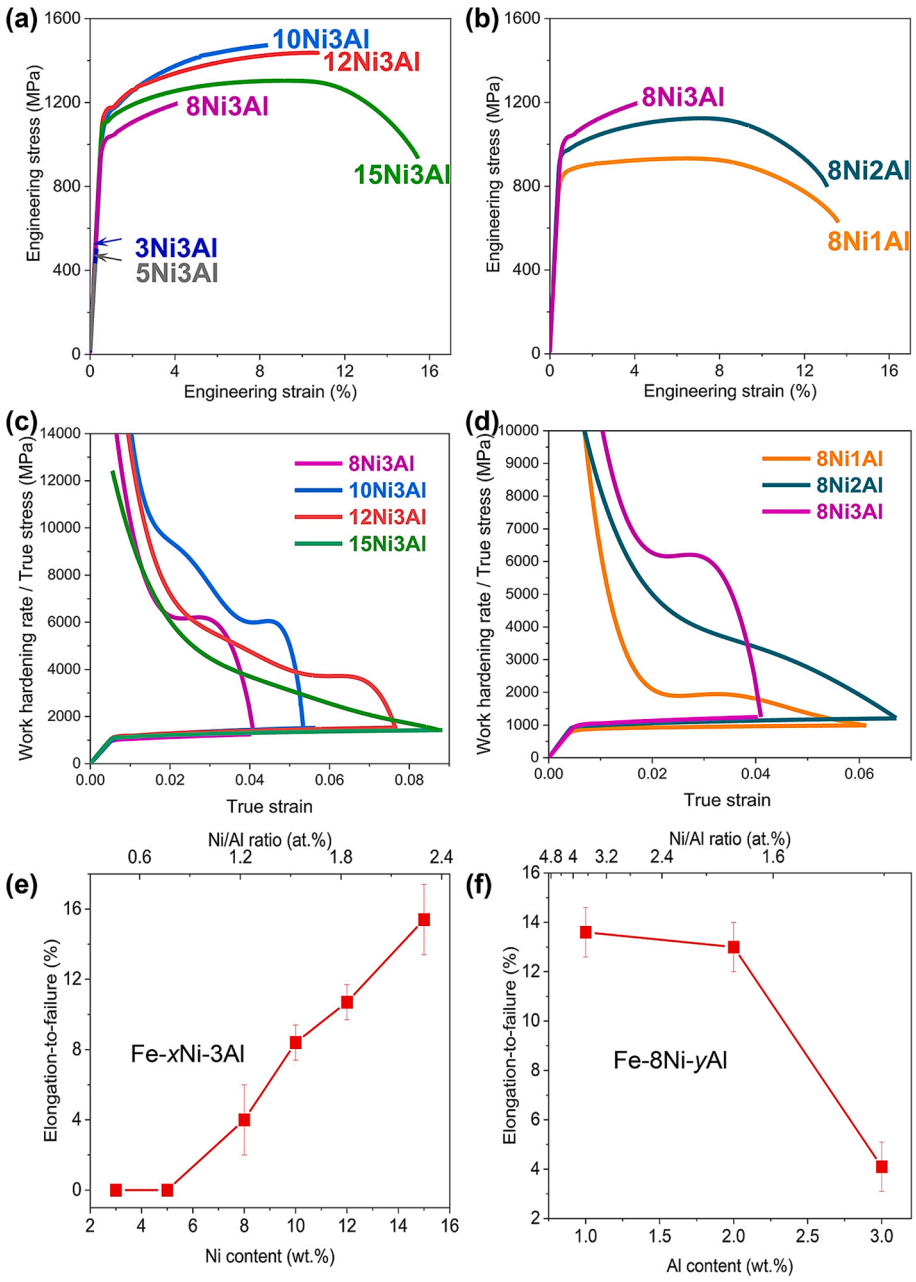

Fig. 7. Engineering stress–strain curves of the (a) Fe–*x*Ni–3Al and (b) Fe–8Ni–*y*Al steels, work hardening rate and true stress–strain curves of the (c) Fe–*x*Ni–3Al and (d) Fe–8Ni–*y*Al steels, and the elongation-to-failure as a function of (e) Ni and (f) Al contents. It is noted that the 3Ni3Al and 5Ni3Al steels are brittle and may fracture before reaching the yield point.

consumes the solute with aging time, thus in the very beginning of precipitation the solute concentration in the CP matrix composition should be very close to the solute composition in the bulk, because the volume fraction of CP precipitates is extremely small. Therefore, the CP matrix composition in the very beginning of precipitation is approximated as the bulk composition. The DP matrix is in a near-equilibrium state and its composition does not vary significantly with aging time; thus, we used the DP matrix concentration in the 2-h aged condition determined by APT in the calculation. With input values of the Ni and Al concentrations in the CP and DP matrix (see Table 1 and Fig. 4), the chemical driving forces for the DP reaction of the Fe-8Ni-*y*Al and Fe-*x*Ni-3Al steels in the early stage of precipitation were determined and are displayed in Fig. 9. As the Al content increases (Fig. 9a), the chemical driving force for the DP reaction decreases from -40.8 ± 15 J/mol in the 8Ni1Al steel to -161.1 ± 20 J/mol in the 8Ni2Al steel and to -339.8 ± 18 J/mol in the 8Ni3Al steel, demonstrating an enhanced chemical driving force for the growth of DP cells. A similar trend was observed for the Fe-*x*Ni-3Al steels (Fig. 9b), in which the chemical driving force for the DP reaction increases swiftly from -29.3 ± 8 J/mol to -553.3 ± 15 J/mol with the increased Ni concentration from 3% to 10% and rises slightly with the Ni content larger than 10%. Therefore, increasing the Ni and/or Al concentration in the steels accelerates the growth of the DP cells, thus leading to a high fraction of DP regions.

4.2. *Deformation mechanisms in Fe–Ni–Al steels*

The tensile results show that the mechanical properties of the Fe–Ni–Al steels vary significantly with Ni and Al contents and ratios. For a fundamental understanding of the deformation mechanisms, it is significant to investigate the interactions of dislocations with the nanoscale

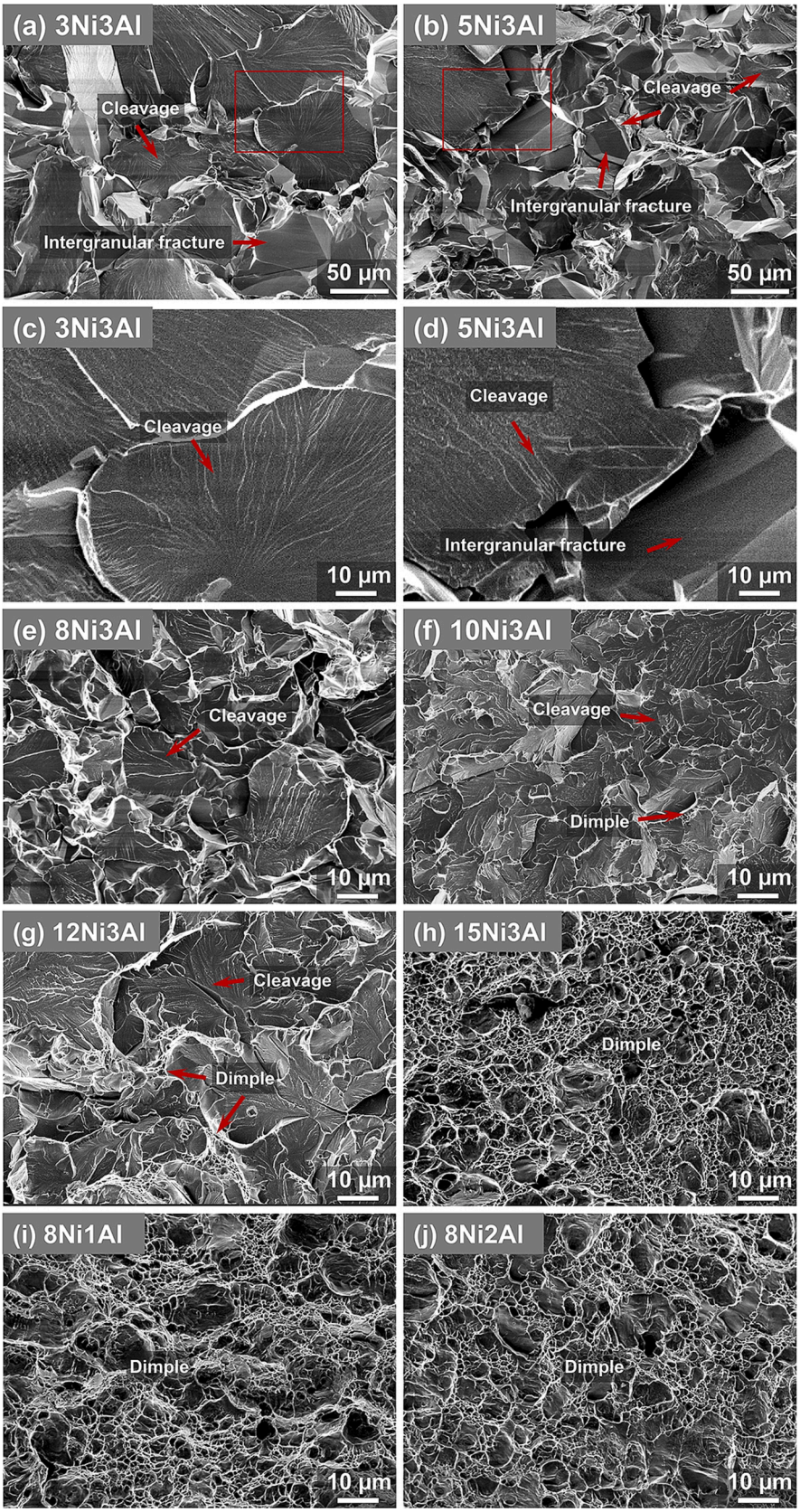

Fig. 8. Fracture surfaces of the Fe-Ni-Al steels: (a,c) 3Ni3Al, (b,d) 5Ni3Al, (e) 8Ni3Al, (f) 10Ni3Al, (g) 12Ni3Al, (h) 15Ni3Al, (i) 8Ni1Al, and (j) 8Ni2Al. (c) and (d) are enlarged view of the regions boxed in (a) and (b), respectively.

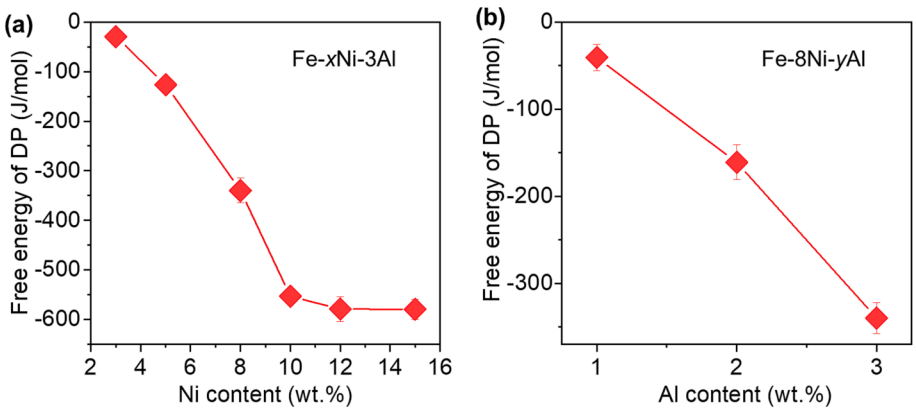

Fig. 9. Calculated chemical driving force for the DP reaction as a function of (a) Ni and (b) Al contents.

precipitates. In this study, the 10Ni3Al and 15Ni3Al steels exhibit similar microstructures but considerably different mechanical properties and work hardening behaviors; thus, these two steels were chosen as representative steels to understand the deformation mechanisms. Fig. 10 illustrates the TEM deformation microstructures of the 10Ni3Al and 15Ni3Al steels at a tensile strain of 8%. It is seen that planar slip is the dominant deformation mechanism in these two steels (Fig. 10a and b). Intersecting planar slip bands are prevalent in the 10Ni3Al steel, whereas straight slip bands dominate in the 15Ni3Al steel. In addition, the interactions of dislocations with the NiAl precipitates were observed. Bright-field and dark-field TEM micrographs of the deformed 10Ni3Al steel are shown in Fig. 10c and e, respectively, and enlarged view of the precipitate-dislocation interaction of the steel and corresponding schematic illustration are shown in Supplementary Fig. S5a and b, respectively. It is evident that the NiAl nano-rods were sheared by dislocations, and the deformation changes the precipitate morphology from long straight rod-like to irregular fragmental shape. For the deformed 15Ni3Al steel, the TEM deformation microstructure images (Fig. 10d and f and Supplementary Fig. S5c) illustrate that the NiAl nano-rods are not sheared by dislocations as observed in the 10Ni3Al steel. Rather, apparent dislocation loops surrounding the NiAl nano-rods were observed, suggesting that the NiAl nano-rods in 15Ni3Al steel are not

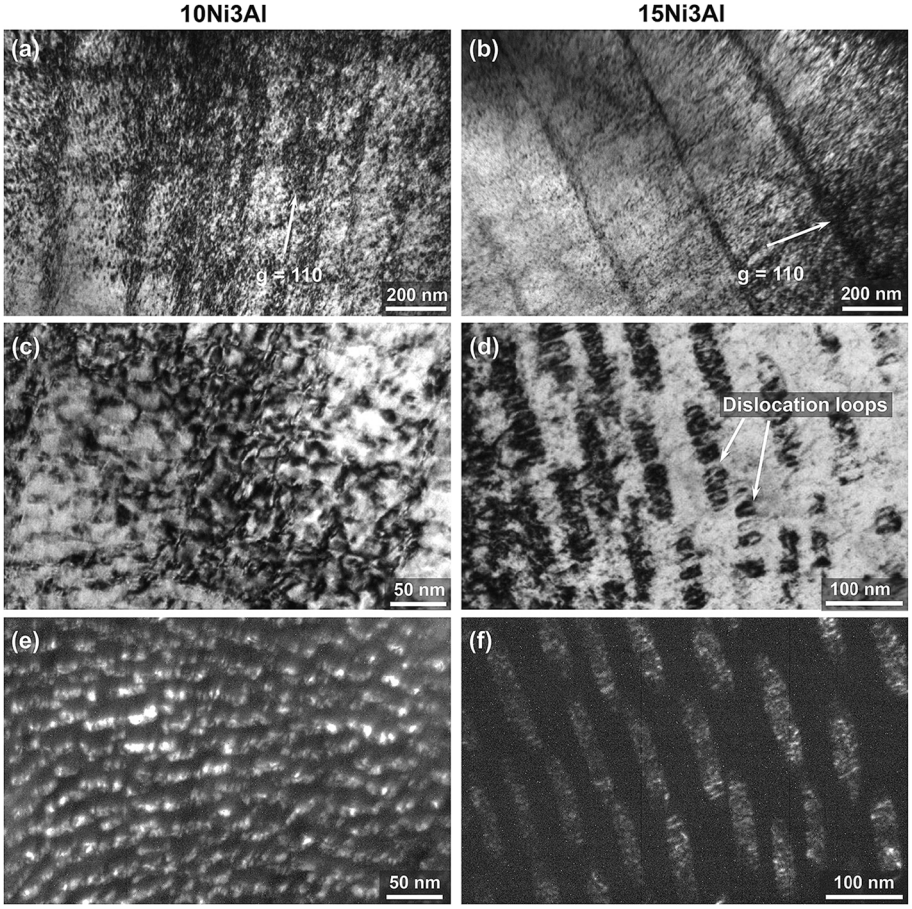

Fig. 10. Deformation microstructures of the (a) 10Ni3Al and (b) 15Ni3Al steels at a tensile strain of 8%. (c) and (e) are bright-field and dark-field images showing the dislocation-precipitate interaction in the 10Ni3Al steel, and (d) and (f) are bright-field and dark-field images showing the dislocation-precipitate interaction in the 15Ni3Al steel.

sheared but bypassed by dislocations during plastic deformation. The above observations indicate that the dislocation-precipitate interaction mechanisms in the 10Ni3Al and 15Ni3Al steels are precipitate shearing and Orowan looping, respectively.

It is well known that the interaction of dislocations with precipitates determines the work hardening behavior and further influences the ductility of precipitation-strengthened materials [36,37]. Our mechanical results indicate that the yield strengths of the 10Ni3Al and 15Ni3Al steels are similar, but the working hardening rate of the 10Ni3Al steel is apparently higher than that of the 15Ni3Al steel (Fig. 7a). Generally, the yield strength is dependent on the precipitate microstructure and the nature of dislocation-precipitate interaction. As the Ni content increases, the volume fraction increases, which is beneficial for strengthening. However, the mode of precipitate-dislocation interaction changes from precipitate shearing to Orowan looping due to the coarsening of the precipitate rods, decreasing the strengthening efficiency. The combined effect of increased volume fraction and decreased strengthening efficiency results in the insignificant change of the yield strength. For the work hardening rate, the NiAl nano-rods of the 10Ni3Al steel are sheared by the dislocations, which leads to the formation of intersecting planar slip bands. The multiplications and interactions of dislocations in the matrix generated during plastic deformation lead to more dislocation storage and form high-density dislocation structures, thereby enhancing the work hardening capability of the 10Ni3Al steel. In addition, compared with the conventional spherical particles, the rod-shaped precipitates can cause an excessive work hardening capability, because the dislocation interactions break the long rod-like precipitates into a high number density of nanoscale fragments, which can become the new barriers to block the motion of dislocations, thus improving the work hardening capability. Consequently, a strong work hardening behavior was observed in the 10Ni3Al steel. For the 15Ni3Al steel with a high concentration of Ni, the NiAl precipitates grow and coarsen rapidly, resulting in the formation of coarse-sized NiAl rods with a small number density. As shown in Fig. 10f, the coarse-sized NiAl rods are non-deformable during plastic deformation. In this material, the dislocation–dislocation interactions are not prevalent, which can be understood from the two aspects: on the one hand, the large inter-precipitate spacing leads to a low dislocation density due to the large dislocation mean free path, which would weaken the ability of strain-hardening [38,39]. On the other hand, the stress increment through work hardening is inversely proportional to the precipitate diameter for conditions where the Orowan looping is operating, as suggested by Ashby [40]. As a result, the 15Ni3Al steel exhibits a low work-hardening behavior. To sum up, the nano-sized NiAl precipitates with a high number density in the 10Ni3Al steel leads to a high work hardening rate through the dislocation shearing mechanism, whereas the coarse-sized NiAl precipitates in the 15Ni3Al steel result in a low work hardening rate through the dislocation bypassing mechanism.

4.3. *Effects of Ni and Al contents and ratios on the ductility of NiAl-strengthened steels*

The mechanical results reveal that the ductility of the Fe–Ni–Al steels is highly dependent on the Ni and Al contents and ratios. Increasing the Ni/Al ratio results in a progressively increased ductility, which is accompanied by the transition of fracture mode from cleavage to dimpled failure. It is commonly understood that microstructure features, such as (1) phase structure, (2) grain size, (3) precipitate microstructure, and (4) matrix composition, can affect the ductility of precipitation-hardened alloys. In the following, the influence of these factors on the ductility of the Fe-Ni-Al steels is critically discussed.

First, we evaluate the effect of phase structure on the ductility of the Fe-Ni-Al steels with different Ni/Al ratios. Because Ni is an austenite stabilizer, it is possible that increasing the Ni content may induce the formation of soft austenite, which can enhance the ductility of the steels [41]. To check this possibility, we examined the phase structure of the Fe–*x*Ni–3Al and Fe–8Ni–*y*Al steels by XRD (Supplementary Fig. S6). For all the studied steels, only peaks corresponding to the ferrite phase were observed, with no detection of any austenite phases. A possible reason for the absence of austenite phase in the high-Ni steels is that most Ni partitions to the NiAl precipitates and the concentration of Ni in the matrix might not be sufficient for the formation of austenite. Therefore, the possibility that the austenite phase improves the ductility of the Fe–Ni–Al steels can be ruled out.

Second, grain size is generally known to be an important factor affecting the ductility and fracture behavior of many crystalline materials, including steels [42–44]. For the propagation of cleavage cracks, the stress that a cracked grain imposes on its neighbors increases with the reciprocal root of the crack length, which is limited by the grain size [12,45,46]. Thus, a coarse grain structure generally results in a low cleavage strength, facilitating the cleavage fracture. In this study, the average grain size of the 3Ni3Al and 5Ni3Al steels is approximately 6 times larger than that of all other steels studied, and these two steels exhibit a cleavage fracture mode with no ductility. Thus, it is likely that grain size is one of the important factors controlling the fracture behavior and ductility of the Fe–Ni–Al steels. On the other hand, we noticed that although the Fe–*x*Ni–3Al steels with $\times$ = 8–15 wt% have similar grain sizes in the range of 9–13 μm, they have significantly different ductilities and fracture modes. This observation indicates that grain size is an important but not the only microstructural parameter determining the ductility; other factors need to be explored.

Third, the precipitate microstructure is known to be a critical parameter determining the deformation behavior and ductility of crystalline materials [22,47,48]. NiAl is an ordered intermetallic compound with high hardness but poor ductility [49], and thus the volume fraction of NiAl precipitates may affect the ductility of materials. Teng *et al.* [21,22] reported that as the volume fraction of NiAl precipitates increases from 4.7% to 18.6%, the bending ductility of NiAl-strengthened ferritic alloys decreases from 5.0% to 1.1%. In this study, the volume fraction of NiAl precipitates is in a small range (2.7%–9.0%). The influence of the variation of the volume fraction of NiAl precipitates on the ductility of the steels is not very obvious. In addition, the dislocation-precipitate interaction can affect the work hardening behavior. As discussed in Section 4.2, the 10Ni3Al steel shows a higher work hardening capability as compared with the 15Ni3Al steel. However, the 10Ni3Al steel is less ductile than the 15Ni3Al steel, which can not be explained by the dislocation-precipitate interaction. Therefore, the dislocation-precipitate interaction is an important but not the dominant factor affecting the ductility of the Fe–Ni–Al steels.

Fourth, we analyzed the effect of matrix composition on the ductility of the Fe–Ni–Al steels. As summarized in Figs. 4 and 6, the Ni and Al concentrations in the matrix vary significantly among the steels, which can influence the intrinsic mechanical properties of the matrix, such as the bulk modulus (B) and shear modulus (G). Generally, the ductility or brittleness nature of a solid material can be evaluated through Pugh's criterion on the B/G ratio [50–53]. A high bulk modulus indicates a strong binding strength, whereas a high shear modulus represents a large resistance to plastic deformation [54,55]. Thus, a high B/G ratio is typically associated with good ductility, whereas a low value corresponds to a brittle nature. To understand the effect of Ni and Al concentrations on the B/G ratio, we performed the first-principles calculations of the Fe–Ni–Al system. Nine 32-atom supercells of BCC-Fe with different Ni and Al contents were constructed. The supercell structures of the Fe_{32}, $Fe_{31}Ni_1$, $Fe_{30}Ni_2$, $Fe_{29}Ni_3$, $Fe_{28}Ni_4$, $Fe_{31}Al_1$, $Fe_{30}Al_2$, $Fe_{29}Al_3$, and $Fe_{28}Al_4$ models were constructed, and the calculated B/G ratios are plotted in Fig. 11 as a function of Ni and Al concentrations. It is evident that the B/G ratio increases significantly with increasing Ni concentration but decreases with increasing Al concentration. From the APT composition, the Ni concentration in the matrix increases monotonously from 2.1 ± 0.1 at.% in the 3Ni3Al steel to 5.5 ± 0.2 at.% in the 15Ni3Al steel, whereas the Al concentration decreases from 5.2 ± 0.1 at.% in the 3Ni3Al steel to 1.5 ± 0.1 at.% in the 15Ni3Al

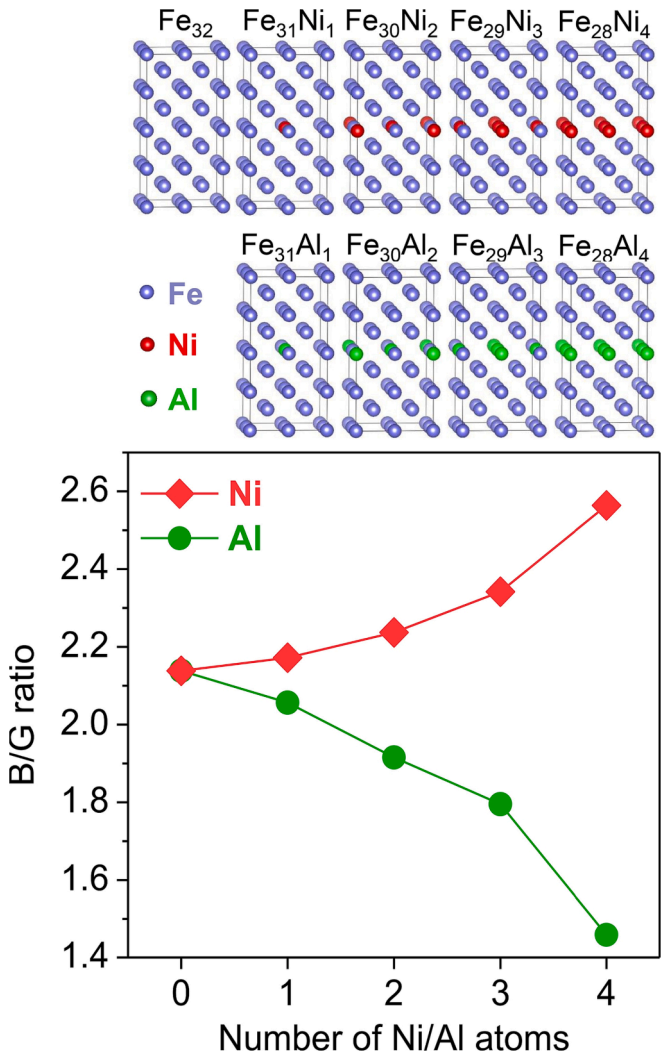

Fig. 11. Supercells of the Fe_{32}, $Fe_{31}Ni_1$, $Fe_{30}Ni_2$, $Fe_{29}Ni_3$, $Fe_{28}Ni_4$, $Fe_{31}Al_1$, $Fe_{30}Al_2$, $Fe_{29}Al_3$, and $Fe_{28}Al_4$ models, and calculated B/G ratios as a function of Ni and Al concentrations.

steel. The increased Ni/Al ratio in the matrix should increase the B/G ratio, which can contribute to the improved ductility of the Fe–Ni–Al steels. This agrees well with our experimental observation that the ductility of the Fe-*x*Ni-3Al steels increases with the Ni content and that of the Fe-8Ni-*y*Al decreases with the Al content. On the basis of the aforementioned discussion, it indicates that multiple parameters including the grain size, precipitate microstructure, and matrix composition affect the ductility of the Fe–Ni–Al steels. Among these factors, the matrix composition plays a crucial role, which can significantly affect the intrinsic ductile nature of the matrix.

5. Conclusions

In this study, we systematically investigated the effects of Ni and Al contents and ratios on the precipitate microstructure, mechanical properties, and fracture behavior of NiAl-strengthened steels with a wide range of compositions. The following conclusions can be drawn from the study:

1. The precipitate microstructure is very sensitive to the Ni and Al contents. Increasing the Ni and Al contents enhances the chemical potential gradient across the reaction front, which increases the chemical driving force for the DP growth, thereby leading to high volume fractions of DP regions. In addition, increasing the Ni/Al ratio results in a refinement of grain size, which provides more nucleation sites for the DP initiation. Consequently, the DP microstructure prevails in the steels with high Ni and Al contents.
2. The deformation behavior of the Fe–Ni–Al steels is highly dependent on the precipitate size and related dislocation-precipitate interaction. The TEM results suggest that fine-sized precipitates are sheared by dislocations, which leads to the formation of intersecting slip bands, resulting in a high work hardening capability. In contrast, the coarse-sized precipitates with a large inter-precipitate spacing are bypassed by the dislocations, leading to a low rate of dislocation storage and hence a low work hardening capability.
3. The Ni and Al contents and ratios also have a significant impact on the mechanical properties of the NiAl-strengthened steels, especially the ductility. Increasing the Ni/Al ratio improves the ductility and changes the fracture mode from cleavage to dimpled failure, whereas decreasing the Ni/Al ratio has an opposite effect. The first-principles calculations indicate that increasing the Ni/Al ratio of the matrix raises the B/G ratio, which can improve the intrinsic ductile nature of the matrix, thereby improving the ductility of the NiAl-strengthened steels. Additionally, decreasing the Ni/Al ratio results in large grain sizes and low B/G ratios of the matrix deteriorates the ductility of the steels.

Declaration of Competing Interest

The authors declare that they have no known competing financial interests or personal relationships that could have appeared to influence the work reported in this paper.

Data availability

Data will be made available on request.

Acknowledgements

This research was supported by the National Natural Science Foundation of China (52171162, 51801169, 51901013 and 52071023), Shenzhen Science and Technology Program (JCYJ20210324142203009), Research Grants Council of Hong Kong (25202719, 15227121, C1017-21GF, and C1020-21GF), State Key Laboratory for Advanced Metals and Materials Open Fund (2021-ZD04), Research Institute for Advanced Manufacturing (P0041364 and P0046108), and PolyU funds (P0038814, P0039624, P0042933, and P0043467).

Appendix A. Supplementary data

Supplementary data to this article can be found online at https://doi.org/10.1016/j.matdes.2023.112341.

References

[1] H. Li, Y. Liu, B. Liu, D.X. Wei, Synergistic enhancement of strength and ductility of cobalt-free maraging steel via nanometer-scaled microstructures, Mater. Sci. Eng. A 842 (2022), 143099.
[2] W. Song, W. Zhang, J. von Appen, R. Dronskowski, W. Bleck, κ-phase formation in Fe–Mn–Al–C austenitic steels, Steel Res. Int. 86 (10) (2015) 1161–1169.
[3] S.S. Xu, J.P. Li, Y. Cui, Y. Zhang, L.X. Sun, J. Li, J.H. Luan, Z.B. Jiao, X.L. Wang, C. T. Liu, Z.W. Zhang, Mechanical properties and deformation mechanisms of a novel austenite-martensite dual phase steel, Int. J. Plast 128 (2020), 102677.
[4] A.K. Singh, D.K. Chouhan, B. Bhattacharya, S. Biswas, High strength-ductility combination by quenching and partitioning of a low carbon microalloyed dual-phase steel, Mater. Sci. Eng. A 870 (2023), 144854.
[5] W. Fu, C. Li, R. Duan, H.S. Gao, X.J. Di, D.P. Wang, Formation mechanism of CuNiAl-rich multi-structured precipitation and its effect on mechanical properties for ultra-high strength low carbon steel obtained via direct quenching and tempering process, Mater. Sci. Eng. A 833 (2022), 142567.

[6] Z.B. Jiao, J.H. Luan, M.K. Miller, Y.W. Chung, C.T. Liu, Co-precipitation of nanoscale particles in steels with ultra-high strength for a new era, Mater. Today 20 (3) (2017) 142–154.
[7] G. Song, Z.Q. Sun, J.D. Poplawsky, Y.F. Gao, P.K. Liaw, Microstructural evolution of single Ni2TiAl or hierarchical NiAl/Ni2TiAl precipitates in Fe-Ni-Al-Cr-Ti ferritic alloys during thermal treatment for elevated-temperature applications, Acta Mater. 127 (2017) 1–16.
[8] Y.R. Wen, A. Hiraata, Z.W. Zhang, T. Fujuta, C.T. Liu, J.H. Jiang, M.W. Chen, Microstructure characterization of Cu-rich nanoprecipitates in a Fe-2.5Cu-1.5Mn-4.0Ni-1.0Al multicomponent ferritic alloy, Acta Mater. 61 (6) (2013) 2133–2147.
[9] S.S. Xu, Y. Zhao, D. Chen, L.W. Sun, L. Chen, X. Tong, C.T. Liu, Z.W. Zhang, Nanoscale precipitation and its influence on strengthening mechanisms in an ultra-high strength low-carbon steel, Int. J. Plast 113 (2019) 99–110.
[10] A.R.H. Far, S.H.M. Anijdan, S.M. Abbasi, The effect of increasing Cu and Ni on a significant enhancement of mechanical properties of high strength low alloy, low carbon steels of HSLA-100 type, Mater. Sci. Eng. A 746 (2019) 384–393.
[11] S.H. Jiang, H. Wang, Y. Wu, X.J. Liu, H.H. Chen, M.J. Yao, B. Gault, D. Ponge, D. Raabe, A. Hirata, M.W. Chen, Y.D. Wang, Z.P. Lu, Ultrastrong steel via minimal lattice misfit and high-density nanoprecipitation, Nature 544 (7691) (2017) 460–464.
[12] S.H. Jiang, X.Q. Xu, W. Li, B. Peng, Y. Wu, X.J. Liu, H. Wang, X.Z. Wang, Z.P. Lu, Strain hardening mediated by coherent nanoprecipitates in ultrahigh-strength steels, Acta Mater. 213 (2021), 116984.
[13] Y. Chen, Q.H. Fang, S.H. Luo, F. Liu, B. Liu, Y. Liu, Z.W. Huang, P.K. Liaw, J. Li, Unraveling a novel precipitate enrichment dependent strengthening behaviour in nickel-based superalloy, Int. J. Plast 155 (2022), 103333.
[14] L. Fan, T. Yang, Y.L. Zhao, J.H. Luan, G. Zhou, H. Wang, Z.B. Jiao, C.T. Liu, Ultrahigh strength and ductility in newly developed materials with coherent nanolamellar architectures, Nat. Commun. 11 (1) (2020) 6240.
[15] L.Y. Liu, Y. Zhang, J.P. Li, M.Y. Fan, X.Y. Wang, G.C. Wu, Z.B. Yang, J.H. Luan, Z. B. Jiao, C.T. Liu, P.K. Liaw, Z.W. Zhang, Enhanced strength-ductility synergy via novel bifunctional nano-precipitates in a high-entropy alloy, Int. J. Plast 153 (2022), 103235.
[16] X.Y. Zhang, J.L. Wang, S.Y. Liu, L. Yan, C.H. Song, H. Yu, Developing NiAl-strengthened HSLA steels by controlling nanoscale precipitation and high-angle boundaries, Mater. Sci. Eng. A 861 (2022), 144355.
[17] Y.R. Wen, L.N. Liang, F.K. Chiang, F. Gao, H.R. Bai, H. Wang, K. Lin, D.D. Xiao, W. J. Qiang, Influences of manganese content and heat treatment on mechanical properties of precipitation-strengthened steels, Mater. Sci. Eng. A 837 (2022), 142724.
[18] M. Kapoor, D. Isheim, G. Ghosh, S. Vaynman, M.E. Fine, Y.W. Chung, Aging characteristics and mechanical properties of 1600 MPa body-centered cubic Cu and B2-NiAl precipitation-strengthened ferritic steel, Acta Mater. 73 (2014) 56–74.
[19] K. Cho, K. Ikeda, H.Y. Yasuda, Improvement of room and high temperature tensile properties of NiAl-strengthened ferritic heat-resistant steels through Mo addition, Mater. Sci. Eng. A 728 (2018) 239–250.
[20] R. Taillard, A. Pineau, Room temperature tensile properties of Fe-19wt.% Cr alloys precipitation hardened by the intermetallic compound NiAl, Mater. Sci. Eng. 56 (3) (1982) 219–231.
[21] Z.K. Teng, C.T. Liu, G. Ghosh, P.K. Liaw, M.E. Fine, Effects of Al on the microstructure and ductility of NiAl-strengthened ferritic steels at room temperature, Intermetallics 18 (8) (2010) 1437–1443.
[22] Z.K. Teng, C.T. Liu, M.K. Miller, G. Ghosh, E.A. Kenik, S. Huang, P.K. Liaw, Room temperature ductility of NiAl-strengthened ferritic steels: Effects of precipitate microstructure, Mater. Sci. Eng. A 541 (2012) 22–27.
[23] Z.W. Zhang, C.T. Liu, M.K. Miller, X.L. Wang, Y.R. Wen, T. Fujita, A. Hirata, M. W. Chen, G. Chen, B.A. Chin, A nanoscale co-precipitation approach for property enhancement of Fe-base alloys, Sci. Rep. 3 (1) (2013) 1–6.
[24] B.C. Zhou, T. Yang, G. Zhou, H. Wang, J.H. Luan, Z.B. Jiao, Mechanisms for suppressing discontinuous precipitation and improving mechanical properties of NiAl-strengthened steels through nanoscale Cu partitioning, Acta Mater. 205 (2021), 116561.
[25] Z.B. Jiao, J.H. Luan, M.K. Miller, C.Y. Yu, C.T. Liu, Effects of Mn partitioning on nanoscale precipitation and mechanical properties of ferritic steels strengthened by NiAl nanoparticles, Acta Mater. 84 (2015) 283–291.
[26] Y. Li, W. Li, N. Min, H.B. Liu, X.J. Jin, Homogeneous elasto-plastic deformation and improved strain compatibility between austenite and ferrite in a co-precipitation hardened medium Mn steel with enhanced hydrogen embrittlement resistance, Int. J. Plast 133 (2020), 102805.
[27] G. Kresse, J. Hafner, Ab initio molecular-dynamics simulation of the liquid-metal–amorphous-semiconductor transition in germanium, Phys. Rev. B 49 (20) (1994) 14251.
[28] G. Kresse, J. Furthmüller, Efficient iterative schemes for ab initio total-energy calculations using a plane-wave basis set, Phys. Rev. B 54 (16) (1996) 11169.
[29] G. Kresse, D. Joubert, From ultrasoft pseudopotentials to the projector augmented-wave method, Phys. Rev. B 59 (3) (1999) 1758.
[30] D.B. Williams, E.P. Butler, Grain boundary discontinuous precipitation reactions, Int. Metals Rev. 26 (1) (1981) 153–183.
[31] P. Zięba, M. Faryna, M. Chronowski, Combined in situ and EBSD studies of discontinuous precipitation in Al-22 at.% Zn alloy, Mater Charact 157 (2019), 109889.
[32] A. Devaraj, L. Kovarik, E. Kautz, B. Arey, S. Jana, C. Lavender, V. Joshi, Grain boundary engineering to control the discontinuous precipitation in multicomponent U10Mo alloy, Acta Mater. 151 (2018) 181–190.
[33] P. Zięba, Recent developments on discontinuous precipitation, Arch. Metall. Mater. 62 (2) (2017) 955–968.
[34] S.H. Kim, H.S. Kim, N.J. Kim, Brittle intermetallic compound makes ultrastrong low-density steel with large ductility, Nature 518 (7537) (2015) 77–79.
[35] J. Petermann, E. Hornbogen, The mechanism of precipitation in lead-sodium solid solutions, Z. Metallkd. 59 (10) (1968) 814–822.
[36] J. Wang, M.X. Yang, X.L. Wu, F.P. Yuan, Achieving better synergy of strength and ductility by adjusting size and volume fraction of coherent κ'–carbides in a lightweight steel, Mater. Sci. Eng. A 857 (2022), 144085.
[37] Q.Z. Gao, C.C. Jiang, H.L. Zhang, Q.S. Ma, H.J. Zhang, Z.Y. Liu, H.J. Li, Co-strengthening of dislocations and precipitates in alumina-forming austenitic steel with cold rolling followed by aging, Mater. Sci. Eng. A 831 (2022), 142181.
[38] M.S. Mehranpour, H. Shahmir, P. Asghari-Rad, M. Hosseinzadeh, N. Rasooli, H. S. Kim, M. Nili-ahmadabadi, Upgrading of superior strength-ductility trade-off of CoCrFeNiMn high-entropy alloy by microstructural engineering, Mater. 22 (2022), 101394.
[39] M.A. Meyers, K.K. Chawla (Eds.), Mechanical Behavior of Materials, Cambridge University Press, 2008.
[40] M. Ashby, Work hardening of dispersion-hardened crystals, Phil. Mag. 14 (132) (1966) 1157–1178.
[41] B.L. Ennis, E. Jimenez-Melero, E.H. Atzema, M. Krugla, M.A. Azeem, D. Rowley, D. Daisenberger, D.N. Hanlon, P.D. Lee, Metastable austenite driven work-hardening behaviour in a TRIP-assisted dual phase steel, Int. J. Plast 88 (2017) 126–139.
[42] J.H. Gao, S.H. Jiang, H.R. Zhang, Y.H. Huang, D. Guan, Y.D. Xu, S.K. Guan, L. A. Bendersky, A.V. Davydov, Y. Wu, H.H. Zhu, Y.D. Wang, Z.P. Lu, W.M. Rainforth, Facile route to bulk ultrafine-grain steels for high strength and ductility, Nature 590 (7845) (2021) 262–267.
[43] C. Pelligra, J. Samei, J.D. Kang, D.S. Wilkinson, The effect of vanadium on microstrain partitioning and localized damage during deformation of unnotched and notched DP1300 steels, Int. J. Plast 158 (2022), 103435.
[44] P.A. Ferreirós, U.A. Sterin, P.R. Alonso, A.J. Knowles, G.H. Rubiolo, Influence of precipitate and grain sizes on the brittle-to-ductile transition in Fe–Al–V bcc-L21 ferritic superalloys, Mater. Sci. Eng. A 856 (2022), 144031.
[45] A.H. Cottrell, Theory of brittle fracture in steel and similar metals, Trans. Met. Soc. AIME 212 (1958).
[46] F. Yanagimoto, T. Hemmi, Y. Suzuki, Y. Takashima, T. Kawabata, K. Shibanuma, Contribution of grain size to resistance against cleavage crack propagation in ferritic steel, Acta Mater. 177 (2019) 96–106.
[47] S.Y. Liu, J.Y. Zhang, H. Zhang, H. Xue, H. Wang, G. Liu, J. Sun, Trifunctional Laves precipitates enabling dual-hierarchical FeCrAl alloys ultra-strong and ductile, Int. J. Plast 159 (2022), 103438.
[48] D.G. Liu, H. Ding, D. Han, M.H. Cai, Effect of grain interior and grain boundary κ-carbides on the strain hardening behavior of medium-Mn lightweight steels, Mater. Sci. Eng. A 871 (2023), 144861.
[49] J. Albiez, H. Erdle, D. Weygand, T. Böhlke, A gradient plasticity creep model accounting for slip transfer/activation at interfaces evaluated for the intermetallic NiAl-9Mo, Int. J. Plast 113 (2019) 291–311.
[50] S.F. Pugh, XCII. Relations between the elastic moduli and the plastic properties of polycrystalline pure metals, Phil. Mag. 45 (367) (1954) 823–843.
[51] W.W. Xu, Z.Y. Xiong, Z.N. Li, X. Gao, W. Li, T. Yang, X.Q. Li, L. Vitos, C.T. Liu, Atomic origins of the plastic deformation micro-mechanisms of γ/γ' FeCoNiAlTi high-entropy alloys, Int. J. Plast 158 (2022), 103439.
[52] O.N. Senkov, D.B. Miracle, S. Rao, Correlations to improve room temperature ductility of refractory complex concentrated alloys, Mater. Sci. Eng. A 820 (2021), 141512.
[53] G. Dirras, L. Lilensten, P. Djemia, M. Laurent-Brocq, D. Tingaud, J.P. Couzinié, L. Perrière, T. Chauveau, I. Guillot, Elastic and plastic properties of as-cast equimolar TiHfZrTaNb high-entropy alloy, Mater. Sci. Eng. A 654 (2016) 30–38.
[54] O.N. Senkov, D.B. Miracle, Generalization of intrinsic ductile-to-brittle criteria by Pugh and Pettifor for materials with a cubic crystal structure, Sci. Rep. 11 (1) (2021) 1–4.
[55] G.S. Wang, S. Schönecker, S. Hertzman, Q.M. Hu, B. Johansson, S.K. Kwon, L. Vitos, Ab initio prediction of the mechanical properties of alloys: The case of Ni/Mn-doped ferromagnetic Fe, Phys. Rev. B 91 (22) (2015), 224203.